Modeling the electric field of weakly electric fish

David Babineau[1], André Longtin[1] and John E. Lewis[2,*]

[1]Department of Physics and [2]Department of Biology, University of Ottawa, Ottawa, Ontario K1N 6N5, Canada

*Author for correspondence (e-mail: jlewis@uottawa.ca)

Summary

Weakly electric fish characterize the environment in which they live by sensing distortions in their self-generated electric field. These distortions result in electric images forming across their skin. In order to better understand electric field generation and image formation in one particular species of electric fish, *Apteronotus leptorhynchus*, we have developed three different numerical models of a two-dimensional cross-section of the fish's body and its surroundings. One of these models mimics the real contour of the fish; two other geometrically simple models allow for an independent study of the effects of the fish's body geometry and conductivity on electric field and image formation. Using these models, we show that the fish's tapered body shape is mainly responsible for the smooth, uniform field in the rostral region, where most electroreceptors are located. The fish's narrowing body geometry is also responsible for the relatively large electric potential in the caudal region. Numerical tests also confirm the previous hypothesis that the electric fish body acts approximately like an ideal voltage divider; this is true especially for the tail region. Next, we calculate electric images produced by simple objects and find they vary according to the current density profile assigned to the fish's electric organ. This explains some of the qualitative differences previously reported for different modeling approaches. The variation of the electric image's shape as a function of different object locations is explained in terms of the fish's geometrical and electrical parameters. Lastly, we discuss novel cues for determining an object's rostro-caudal location and lateral distance using these electric images.

Key words: electric image, electrolocation, finite-element-model, *Apteronotus leptorhynchus*.

Introduction

In order to extract relevant features from the environment in which they live, animals use both active and passive sensing mechanisms. For species that use an active sensing mechanism, the acquisition of sensory information greatly depends on the efferent signal produced, which can be sensitive to environmental influences. Weakly electric fish detect objects and communicate with conspecifics through a unique modality, the active electric sense (Heiligenberg, 1991). This sense relies on an electric organ discharge (EOD) emitted from the fish's electric organ (EO). The EOD can either be continuous and quasi-sinusoidal ('wave-type' species), or discrete and pulse-like ('pulse-type' species). The species studied in this paper, *Apteronotus leptorhynchus*, is a wave-type species with an EOD frequency of approximately 1 kHz. The electric field time course generated by this fish is complex with tri-phasic regions close to the skin, but becomes approximately dipolar further away (Knudsen, 1975; Assad et al., 1999). Objects whose electrical properties differ from those of the surrounding water perturb the fish's electric field (Lissman and Machin, 1958) and are sensed by specialized receptors located within the fish's epidermis. Many studies have shown that these electroreceptors respond to transdermal potential differences rather than to transdermal current (e.g. Bennett, 1971; Migliaro et al., 2005). The rostro-caudal, dorso-ventral profile of the transdermal potential differences is commonly referred to as the 'electric image'. Because these images are the primary source of electrosensory input, a detailed knowledge of the electric field and image formation is required in order to understand the neural mechanisms of electrosensory information processing.

In recent years, different modeling techniques have been used to characterize electric images under various natural scenarios. Two- and three-dimensional numerical and analytical models have been developed, each with its specific advantages and disadvantages. Analytical models (e.g. Bacher, 1983; Chen et al., 2005), while being computationally fast and accurate in some cases, are limited to the study of simplified object geometries and also do not allow for a thorough study of the effects of the fish's body parameters. Numerical models (e.g. Hoshimiya et al., 1980; Assad, 1997; Rother et al., 2003) can mimic the fish's body in a more realistic way, yet are considered more computationally time-demanding. The two main methods used in numerical modeling are the finite element method (FEM) and the boundary element method

(BEM). The BEM is advantageous because only the solution at the boundaries is necessary (e.g. at the fish–water interface), therefore reducing the number of calculations and allowing for three-dimensional models (Assad, 1997; Rother et al., 2003). Three-dimensional FEM models are currently not practical in general due to the large number of elements required to accurately represent, for example, the crucial thin skin layer. On the other hand, the BEM requires additional calculations to find potentials on non-boundary regions and is harder to implement than the FEM (e.g. boundary integrals are more difficult to evaluate and not all linear problems can be treated) (Yamashita, 1990; Assad, 1997).

The goal of this paper was to study the fish in a realistic and accurate manner, using a fast and easily-implementable model. Taking advantage of improved computational power and software, a morphologically realistic two-dimensional FEM model, which is both computationally fast and easy to implement, was created. In addition to the realistic model created, two geometrically simple models were also created in order to independently study the effects of different fish body geometries and electrical properties for the first time. Using the three distinct models, an analysis of the fish's mid-planar field (view from above) and of the electric images caused by objects of different sizes and locations is presented. This study complements other recent studies that have begun to characterize the fish's electric field and electric image formation using different approaches (Caputi and Budelli, 1995; Caputi et al., 1998; Rother et al., 2003; Migliaro et al., 2005; Chen et al., 2005). In addition, our approach allows for future modeling efforts involving realistic electrosensory landscapes.

Materials and methods
Electric field modeling

The two-dimensional, horizontal midplane electric field potential of *Apteronotus leptorhynchus* (Eigenmann) was modeled for a single phase (head-positive). As in previous studies (Rasnow et al., 1989; Assad, 1997), the problem was treated as an electrostatics boundary-value problem, governed by Poisson's equation,

$$\nabla \cdot \sigma \nabla \Phi = -j \,, \qquad (1)$$

where Φ is the potential (in V), j is the current source density (in A m^{-3}) and σ is the conductivity (in S m^{-1}) (each defined for all points in the two-dimensional plane). This equation was solved using finite element method (FEM) software, COMSOL Multiphysics (formerly known as FEMLAB) on an IBM computer with a 3.2 GHz Intel Xeon processor. The current source density units are in A m^{-3} because COMSOL Multiphysics treats the problem as a three-dimensional problem in which the model has a 1 m thickness in the *z*-direction. In this manner, the model is 'thick' enough to neglect variations in the *z*-direction. Second-order Lagrange elements (triangles) were used in the finite element mesh. We chose a pre-defined mesh mode ('normal' mode), which automatically selected element sizes based on the size of the objects located within the geometry. This mode typically produced meshes with ~90 000 elements. In order to calibrate the software, we studied a simple problem whose analytical solution is known: a line charge in the middle of a grounded tube. We found an RMS error of 0.27% (Babineau, 2006).

Our studies involve three different fish geometries: one morphologically accurate model (referred to as the 'fish' model) and two greatly simplified models (referred to as the 'taper' and 'box' models; see later for descriptions). Each model is enclosed in a 70×70 cm^2 aquarium, which also holds grounding and reference electrodes (Fig. 1A). The size, location and conductivity of these components correspond to those found in Assad's experimental setup (Assad, 1997), with whose experimental data we calibrated our fish model.

Morphologically accurate fish model

For the fish model, the contour of the 21 cm fish was slightly adapted from Assad's original mapping by removing the operculum and by symmetrizing the body contour with respect to the rostro-caudal axis, thereby simplifying the interpretation of our results (Fig. 1B). These modifications did not negatively affect the data fitting, and, in fact, did improve the overall error by approximately 10% (see later for error measurement). The size and shape of the EO was adapted from Moller (Moller, 1995) by approximating the actual shape with an appropriately sized rectangle. The 100-μm thick skin layer was selected as an acceptable upper bound, based on previous measurements (Bennett, 1971; Zakon, 1986). The fish model therefore has three compartments: an EO, a thin skin layer, and a body component located between the EO and the skin. The reference electrode is placed laterally to the fish, while the grounding electrode is placed in the corner of the tank (Assad, 1997). Water conductivity was set to 0.023 S m^{-1} (Assad, 1997), in order to mimic experimental conditions. The potential values were obtained by moving an array of electrodes around an immobilized fish (Assad, 1997). These potentials were differentiated with respect to a fixed electrode located lateral to the fish, near the fish's zero-potential line (see Fig. 1A).

Electric field model parameters

Four of the fish model's parameters were varied systematically in order to minimize the error between the simulated and measured potential fields: skin, body and EO conductivity, as well as EO current density profile. EO conductivity was varied from 0.01 to 100 S m^{-1}, body conductivity from 0.01 to 10 S m^{-1}, and uniform skin conductivity from 0.00001 to 10 S m^{-1}. A non-uniform skin conductivity profile, as predicted by several studies (Heiligenberg, 1975; Hoshimiya et al., 1980; Assad, 1997), was also tested. This profile had three parts: a head conductivity of 0.00025 S m^{-1} (first 60% of body length, *BL*), a tail conductivity of 0.0025 S m^{-1} (last 10% of *BL*) and a mid-body conductivity which varied linearly from 0.00025 to 0.0025 S m^{-1} for the middle 30% of the fish's *BL* (see Fig. 8A). These bulk conductivity values, which depend on skin
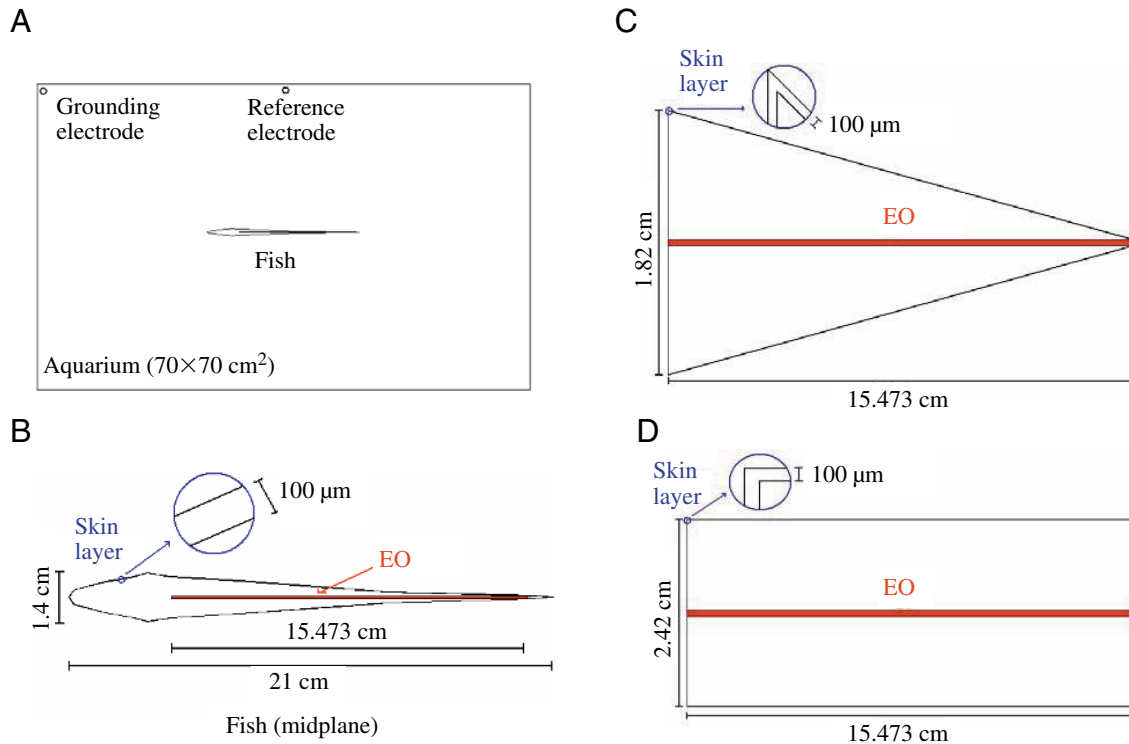
Fig. 1. Electric field models. (A) Complete view of the model geometry, composed of an aquarium, grounding and reference electrodes and the model fish. (B) Close-up of morphologically accurate 'fish' model consisting of a thin skin layer, an electric organ (EO) and an interior body component (between the EO and skin). The EO is 15.47 cm long and 0.08 cm thick, the skin is 0.01 cm thick and the fish is 21cm long and 1.4 cm wide. (C,D) Geometrically simple models used for studying (C) different fish tapers (see text for explanation) and (D) various body and skin properties. To achieve different tapers in C, the left side of the model (here shown for a width of 1.82 cm) is varied. The EO length and skin thickness for C and D are the same as in B. Model C is referred to as the 'taper' model and model D is referred to as the 'box' model. x and y axes, as well as grounding and reference electrodes, are not to scale.

thickness, were re-calculated from Assad (Assad, 1997) for our chosen skin thickness of 100 μm (*versus* 200 μm). Assad had chosen 200 μm as a conservative assumption, but we have reduced the skin thickness in order to more accurately mimic values found in the literature, as noted previously.

For the head-positive phase of the EOD cycle studied in the present work, the potential changes polarity along the EO from positive at the fish's head to negative at the tail. In addition, the field is positive for most of the body length and is much stronger (negative) in the tail (see Fig. 3A). Thus, several zero-mean, bimodal EO current density profiles (linear profile, two component point-line EO, etc.) were tested in order to mimic this field. One profile, however, allowed for a more thorough investigation due to its general nature and amenability to mimic various EOD phases. This current density profile, referred to as 'skewed' in this paper, is composed of two Gaussian curves: a rostral positive one and a caudal negative one (see Fig. 2A). Such a current density was chosen for its generality; knowledge of the exterior field cannot uniquely determine the distribution of sinks and sources inside of the fish (Rasnow and Bower, 1996), and experimental data is currently unavailable.

In order to find the optimal skewed current density parameters, reasonable estimates for the conductivities of the three separate fish compartments were initially assumed (EO: 1 S m^{-1}, body: 1 S m^{-1}, skin: previously mentioned non-uniform profile) (Scheich and Bullock, 1974; Assad, 1997). The mean and standard deviation of the two Gaussian curves that make up the skewed profile were also initially adjusted in order to mimic the approximately dipolar field. Afterwards, these four current density parameters were altered sequentially in order to minimize the model's error (see next section for error measure). For every set of current density parameters varied, the amplitudes of the two Gaussian curves were adjusted in order to make the mean of the skewed profile as close to zero as possible. This was accomplished by optimizing the rostral curve's amplitude while fixing the caudal curve's amplitude (hence the rostral curve's amplitude was a fifth free current density parameter). Once each skewed current density profile parameter had been optimized, a standard 'nonlinear grid search' method (Bevington and Robinson, 2003) was applied in order to obtain a more precise value of the optimal parameter. In short, this method entailed finding the minimum of the error parabola generated by the 'optimal' parameter value and the pair of parameter values (less than and greater than the optimal value) for which the model's error increased. Once the EO current density parameters were established, the

EO, body and skin conductivities were varied within the aforementioned ranges and were similarly optimized using the nonlinear grid search method. A second series of optimizations were abandoned since accuracy did not improve greatly.

Model calibration

We calibrated our fish model to experimental data (Assad, 1997) using a weighted RMS error. The weighting was done to put more emphasis on the near field, in the range of active electrolocation (MacIver et al., 2001), and because potential falls off to zero in the far field. The overall, n-node weighted RMS error is given by:

$$\text{RMS (\%)} = 100 \times \sqrt{\frac{1}{\sum\limits_{i}^{n} w_i^2} \sum\limits_{i=1}^{n} w_i^2 \left(\frac{\Phi_i^{\text{sim}} - \Phi_i^{\text{exp}}}{\Phi_i^{\text{exp}}}\right)^2} \quad , \quad (2)$$

where Φ_i^{sim} and Φ_i^{exp} are the simulated and experimental potentials at a given node. The weighting function w_i was a factor proportional to the average rostro-caudal field strength: this factor was set to a maximal value of 1 within 2 cm of the fish's skin and had a minimal value of 0.138 near the lateral tank wall (the w_i were set to one when the non-weighted, standard RMS error was calculated). The nodes used to calculate this weighted error were also re-sampled from 361 to 325 (36 nodes withdrawn) in order to remove any bias caused by the original, uneven data sampling (Assad, 1997). Furthermore, the field images shown in Fig. 3 were generated using these re-sampled nodes.

Geometrically simple electric field models

In order to study independently the effect of fish geometry and electrical conductivities of the different body compartments on the electric field and images, two geometrically simple electric field models were created, differing only in body contour from the fish model. The first geometrically simple model, referred to as the 'taper' model (Fig. 1C), has a triangular body contour that touches the EO at both ends. The value of the taper is given by the ratio of the lateral and horizontal extents of the skin contour (on one of the fish's sides). In order to study a given taper (found along the fish model's outer contour), the rostral lateral segment of the taper model was adjusted appropriately. The second geometrically simple model, referred to as the 'box' model (Fig. 1D), has a rectangular body contour that touches the EO at both ends. The effects of the various body conductivities and of EO-to-skin distance were studied using this model, independent of the effects of taper. For experiments in which the EO-to-skin distance was not varied, a width of 2.42 cm was used by default (see Fig. 1D). Results obtained with various widths were qualitatively the same; therefore, the exact choice of the box's width was not important for the comparative studies conducted in this paper. Uniform conductivity parameters were used in these models (optimal values from the fish model; see Results), unless otherwise stated.

In addition to the optimal skewed EO current density (see

Results), a sinusoidal current density, which held an integer number of wavelengths along the EO, was also tested in these models (profiles with, e.g. 1 or 5 wavelengths, are respectively referred to as '1-cycle' or '5-cycle' sinusoidal waves in this paper). Sinusoidal profiles, which are standard periodic functions, were chosen in order to better compare the results obtained with the more realistic, but skewed current density profile.

Electric field characterization tools

In order to characterize the degree of uniformity or 'smoothness' of the electric field around the fish, a quantitative measure was needed. To this end, we used a measure of 'energy' (proportional to electric energy) to quantify the degree of smoothness of the potential Φ along the EO as well as along the interior and exterior skin boundaries. It is defined as:

$$\text{Energy} = \int \left(\frac{d\Phi}{dx'}\right)^2 dx' \ . \qquad (3)$$

This measure is analogous to the (potential) energy held within a string stretched along a dimension 'x' that is perturbed in the 'y' dimension. When no energy is applied to the string, there is no variation in the vertical dimension (y; analogous to Φ) as a function of the horizontal dimension (x). However, if the string is suddenly moved up and down repeatedly so that, for example, a sinusoidal pattern results, y will change as a function of x (hence $dy/dx \neq 0$), and therefore Eqn 3 yields a non-zero value for energy. In this sense, the 'rougher' the potential variation along a given line is, the higher its associated energy value will be.

To study the electrical filtering effects of the fish body, i.e. how the uniformity of the electric potential profile changes from inside to outside the fish, the energy at the EO level ($\text{Energy}_{\text{EO}}$) was compared with the energy at the exterior ($\text{Energy}_{\text{ext}}$) skin level. This filtering effect was quantified as the percentage of energy lost across the body:

$$\text{Filtering (\%)} = 100 \left(\frac{\text{Energy}_{\text{EO}} - \text{Energy}_{\text{ext}}}{\text{Energy}_{\text{EO}}}\right) . \qquad (4)$$

With higher filtering values, more energy is being lost (filtered) from the EO to the skin exterior. A 50-cycle sinusoidal current density (see previous section) was used in order to calculate filtering. The EO segment was divided into 50 separate sections and one filtering value was calculated per section (i.e. one filtering value per wavelength). This spatial 'frequency', although higher than that of the skewed current density, was selected because it made it possible to visualize the body's filtering effects along the body with good spatial resolution (see e.g. Fig. 4B). Further, we found that the filtering curve's main feature, namely a head-to-tail decrease in filtering, remained the same for all frequencies; only the absolute values differed.

In order to test the accuracy of the electric fish as an ideal voltage divider, we compared the simulated (V_{sim}) and theoretical (V_{theo}) transdermal potentials all along the fish's rostro-caudal axis (x) using the taper model (taper ratio=0.05)

with a 5-cycle sinusoidal current density. The following formula, which stems from the standard 'perfect voltage divider' equation for an unloaded circuit, was used:

$$V_{\text{theo}}(x) = \frac{V_{\text{ext}}(x) - V_{\text{EO}}(x)}{\left(\dfrac{\sigma_{\text{skin}} \cdot t_{\text{body}}(x)}{\sigma_{\text{body}} \cdot t_{\text{skin}}(x)} + 1\right)}, \quad (5)$$

where V_{ext} and V_{EO} are the potentials at the exterior skin level and at the EO level, respectively, σ_{skin} and σ_{body} are the conductivities of the skin and body, respectively, and where t_{skin} and t_{body} are the thicknesses of the skin and body, respectively.

Electric image calculations

Electric images were calculated as the difference between transdermal potentials in the presence (OB) and in the absence (NO) of an object, all along the rostro-caudal axis, as in previous studies (Hoshimiya et al., 1980; Chen et al., 2005; Migliaro et al., 2005):

$$\Delta\Phi(x) = \left[\Phi_{\text{ext}}^{\text{OB}}(x) - \Phi_{\text{int}}^{\text{OB}}(x)\right] - \left[\Phi_{\text{ext}}^{\text{NO}}(x) - \Phi_{\text{int}}^{\text{NO}}(x)\right], \quad (6)$$

where 'ext' and 'int' denote the exterior and interior boundaries of the skin layer, respectively.

Some of the electric images produced by the skewed current density profile used in this paper are generally bimodal in nature; rostral and caudal peaks of differing polarities are present. Throughout our analysis, the potential difference between the two largest peaks will be referred to as the 'peak-to-peak potential', while the horizontal distance between them will be called the 'peak-to-peak distance' or 'delta'. Please note also that the words 'images' and 'electric images' will be used interchangeably throughout the text.

All electric images in this paper were produced by a 1.1 cm-radius metal (brass; conductivity=2.13×10^7 S m^{-1}) disc, unless otherwise stated.

Results

Optimal model parameters

The optimal EO current density is shown in Fig. 2A (red trace). It is defined by a difference of Gaussians: a 'positive', rostral Gaussian curve (blue trace, centered 15 cm from the tip of the head with a standard deviation of 4.46 cm) and a 'negative', caudal Gaussian curve (green trace, centered 18.04 cm from the tip of the head with a standard deviation of 0.5 cm). The ratio of the peak amplitudes, positive to negative, is 1:8.38, respectively. The electric fields generated from other bimodal current densities (see Materials and methods) did not match the measured data as well as with this optimal 'skewed' profile (data not shown).

Fig. 2B shows a sensitivity analysis relative to the optimal (uniform) conductivity values of the different fish compartments. The vertical axis shows error above the minimal weighted RMS error, found with optimal parameters (28.6%); the horizontal axis shows normalized parameter values

(optimal conductivity values each set to one). The optimal parameter values are: EO conductivity, 0.927 S m^{-1}; uniform skin conductivity, 0.0017 S m^{-1}; body conductivity, 0.356 S m^{-1}. Skin conductivity is the least sensitive of the three conductivity parameters. A non-uniform skin conductivity profile was tested as well (see Fig. 8A), giving slightly better results (0.5% less error). Contrary to previous studies, however,
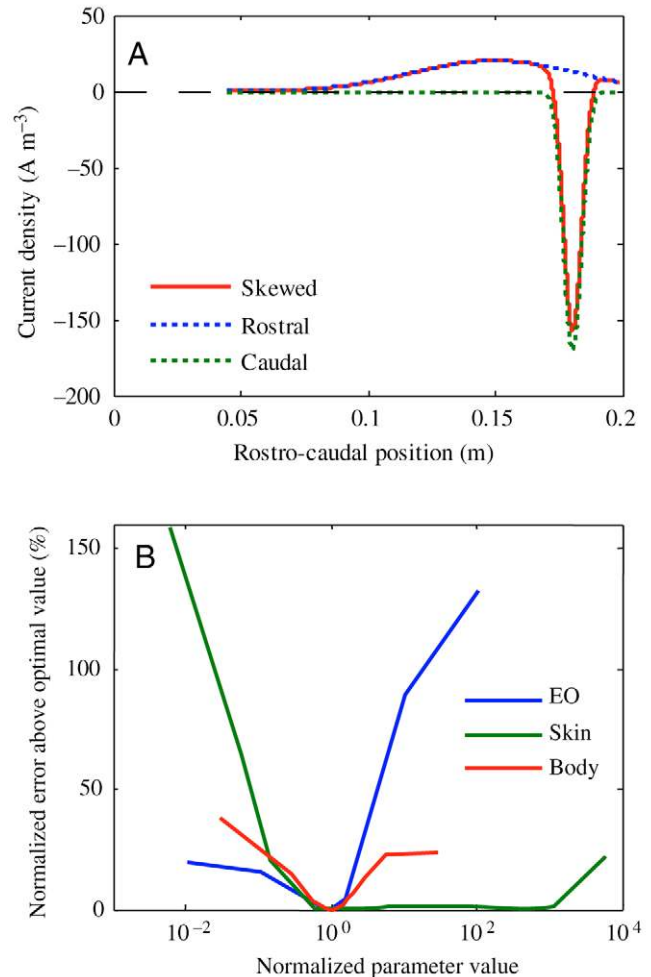

Fig. 2. Optimal model parameters. (A) The optimal EO current density profile (red), called 'skewed', is the sum of two Gaussian curves: a narrow (dotted green) sink in the tail region and a wide (dotted blue) source in the mid-body. Rostral curve is centered 15 cm from the tip of the head and has a standard deviation of 4.46 cm; caudal curve is centered 18.04 cm from the tip of the head and has a standard deviation of 0.5 cm. The ratio of the peak amplitudes of the two curves is 1:8.38. (B) Optimal conductivity values for the EO (blue), skin (green) and body (red). Optimal parameter values are normalized to one and the errors associated with each optimal parameter value are set to zero. Abscissa values are given as ratios of the optimal parameter value (for each respective curve) and ordinate values are given as field RMS% errors above minimal error (28.6%; see text for details on error measure). Optimal conductivity values are: EO, 0.927 S m^{-1}; body, 0.356 S m^{-1}; skin, 0.0017 S m^{-1}. Although all parameters here were varied homogeneously, it should be noted that the optimal skin conductivity is not uniform along the length of the fish (see Fig. 8A).

we did not find that non-uniform skin conductivity was necessary to reproduce the rostrally leaning zero-potential line (not shown). Nevertheless, since the error associated with this type of profile was better, it was used by default throughout this paper, except for when the effects of other parameters were studied independently and hence the optimal uniform skin conductivity was used (see later section).

Model calibration

Fig. 3A shows the measured (top) and simulated (bottom) field potentials (simulated field shown for optimal set of parameters, including non-uniform skin conductivity). Most qualitative aspects of the measured field, such as the uniform potential in the head region, the elongated dipole field shape, and the rostrally leaning zero-potential line, are reproduced. Aspects which are not reproduced as effectively are the high

potential and rate of field decay in the tail region. This can further be seen in Fig. 3C, which shows the absolute potential difference between simulated and experimental data; notice that only the tail region features a discrepancy of several mV (differences over 5 mV are mapped to dark red; maximal difference is ~ 22 mV). Fig. 3B shows the un-weighted RMS error. The error close to the fish is relatively low (~10% in the rostral near field and similar to that of a recent analytical model) (Chen et al., 2005). The error increases further away; this is especially apparent near the zero-potential line, where the measured absolute potentials are very small (μV magnitude; see Fig. 3C), hence creating large relative discrepancies with the simulated field. Fig. 3D,E show the fall-off of potential with lateral distance for two different rostro-caudal locations, one at the head (Fig. 3D) and one at the tail (Fig. 3E). These figures show that even though the error
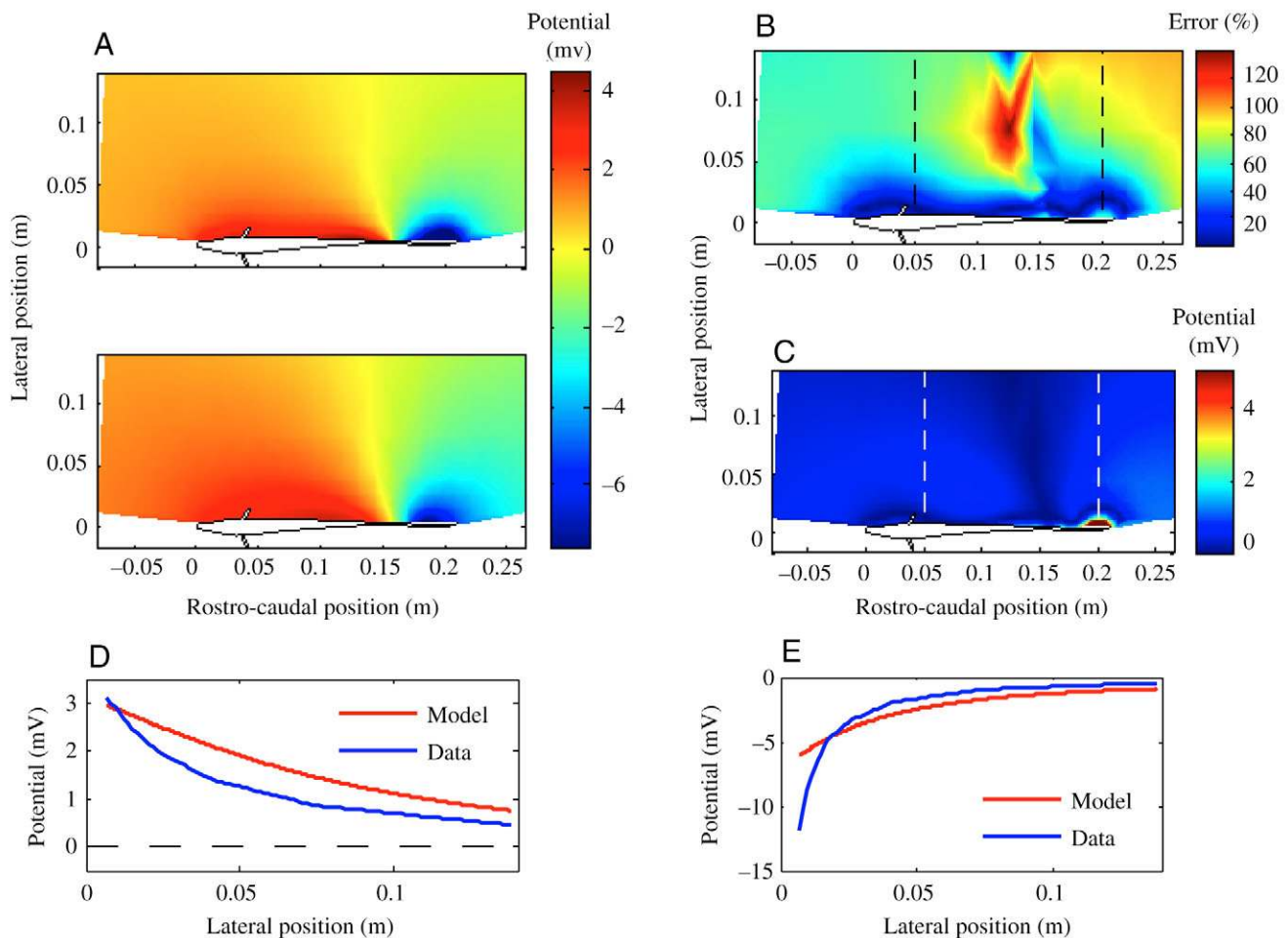

Fig. 3. Model calibration. (A) 2D field potential surrounding the fish. Top: experimental data obtained from Assad (Assad, 1997). Bottom: simulated values obtained with optimal parameters (including non-uniform skin conductivity). Color maps represent potential with respect to an electrode placed laterally to the fish, near its zero-potential line (as in Fig. 1A). All values below approx. –7.6 mV have been mapped to dark blue in order to show a better contrast between the positive and negative regions of the dipolar field (measured potential in tail region reaches approx. –30 mV). The zero-potential line is shown in yellow. (B) Un-weighted % error and (C) absolute potential differences between data and simulated values found in A. Broken lines show cross-sections at which the potentials are plotted in (D) and (E). Potential differences in C greater than 5 mV are all mapped to dark red. (D) Potential along dotted line near head (5 cm caudal from the tip of the head) in B for model (red) and data (blue). (E) Potential along dotted line near tail (20 cm caudal from the tip of the head) in B for model (red) and data (blue).

increases further away (see Fig. 3B), the fall-off is qualitatively similar between our model and the data. The average weighted RMS error is 28%; the average un-weighted RMS error is 43%; the average potential difference over the entire field is approximately 1 mV.

Electric field characterization

Filtering

Previous studies have noted that the electric field in the head region of *A. leptorhynchus* is relatively uniform along the body (Rasnow et al., 1993; Nelson, 2005), but have not investigated its possible origin. In this section, we quantitatively analyze the degree of electric field uniformity and its possible origin for the first time. In Fig. 4A, the potential at the EO level and at the inner and outer skin boundaries of the fish model are shown as a function of normalized EO length (zero corresponding to the

rostral end, one to the caudal end) for a 5-cycle sinusoidal current density. The potential at the fish's exterior is much smoother than at the EO level in the head region, and becomes more spatially heterogeneous, or rougher, towards the tail. This was also apparent for sinusoidal current densities of higher and lower frequencies as well as for other current density profiles (data not shown). The EO potential also increases caudally, due to the 'narrowing' taper of the fish (this is not due to the EO current density, since in this example its amplitude was the same all along the EO).

Fig. 4B further characterizes the smoothness of the exterior potential. The green trace shows that the normalized energy at the exterior skin level approaches a value of zero towards the head, implying that the potential is almost perfectly 'flat' in this region; the energy is minimal in the head region situated to the left of the EO (left of red line). The blue trace shows that
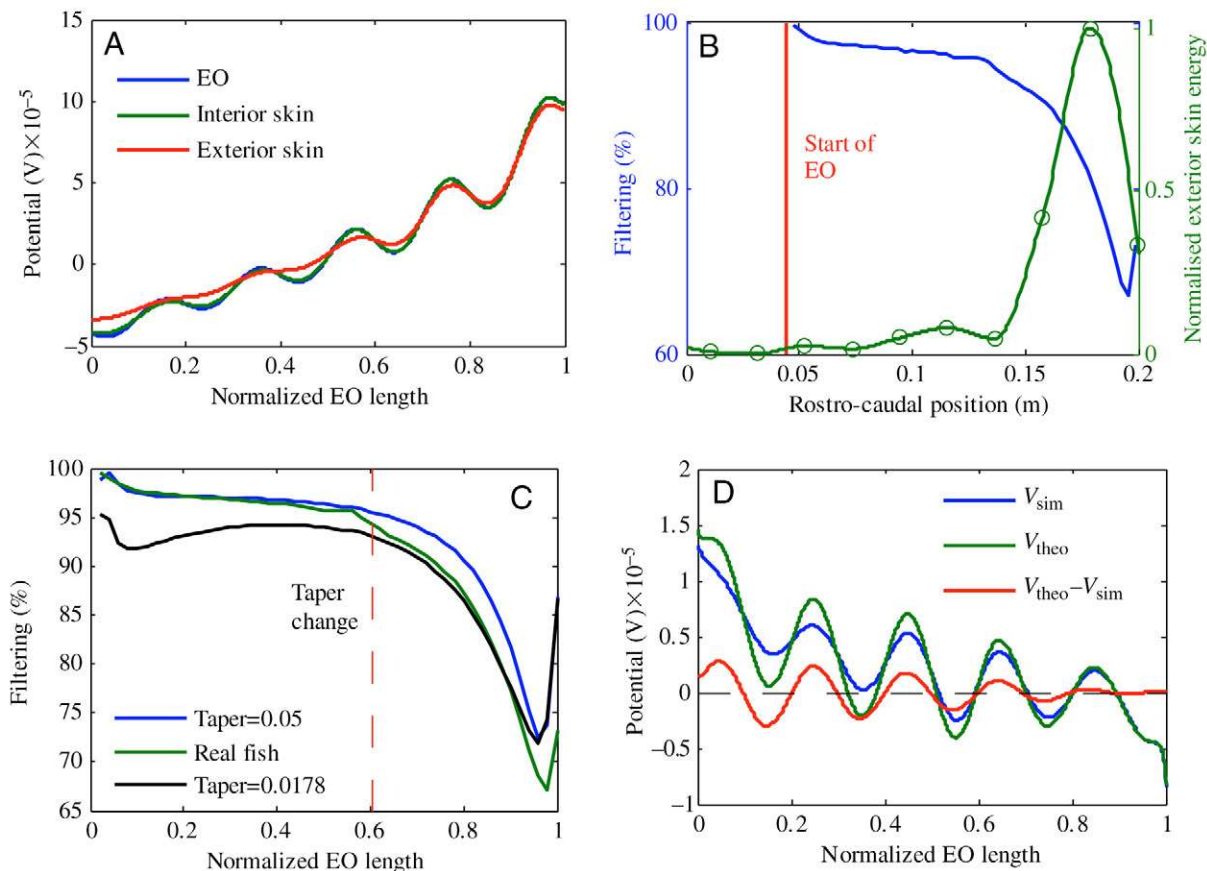

Fig. 4. Electric field characterization: study of the fish's filtering properties and comparison with an ideal voltage divider. (A) Potential values at the electric organ (blue) and at the interior (green) and exterior (red) skin boundaries along the EO segment (zero corresponds to the rostral end, one to the caudal end), for a 5-cycle sinusoidal current density (fish model). (B) Right axis, green trace shows the normalized energy of the exterior skin potential curve as a function of rostro-caudal position along the fish body (fish model; solid line was obtained using the 'shape-preserving interpolant' fitting function in MATLAB). This energy quantifies the level of 'smoothness' of a given trace (see text for details). Left axis, blue trace shows the filtering along the EO segment for a 50-cycle sinusoidal current density (fish model). Filtering quantifies how much the energy has decreased from the EO to the skin (see text for details). The red line represents the start of the EO in the fish model (x=4.42 cm; see Fig. 1B). (C) Filtering along the EO segment for the fish model (green) and for the taper model with low (black) and high (blue) taper values. Red broken line represents the location of taper change in the fish model. (D) Comparison between the fish and an ideal voltage divider (taper model, taper=0.05). Theoretical (green) and simulated (blue) transdermal potentials along the EO segment for a 5-cycle sinusoidal current density. Red trace shows the difference between simulation and theory (see text for details).

filtering is maximal rostrally and decreases caudally, with a mean filtering value of 91.5% (shown for a 50-cycle sinusoidal current density). By contrast, the mean filtering for a 1-cycle sinusoidal current density is 47.3%. Therefore, the mean filtering value obtained with the skewed current density will be in between these two values (recall that a higher frequency was used in order to better visualize filtering along the body axis). While the body and skin tend to filter out more of the potential at higher frequencies, the qualitative shape of the filtering curve obtained with lower frequencies remains the same as in Fig. 4B (not shown).

Several tests with the two geometrically simple models were carried out in order to understand how different parameters affect the filtering due to the fish's body. By comparing the exterior (red trace) and interior (green trace) potentials in Fig. 4A, it is clear that the skin acts as a filter. However, the skin alone cannot account for the head-to-tail drop-off in filtering of nearly 35% in the fish model (see Fig. 4C, green trace). Nor can this effect be explained by the different head and tail conductivities found in the non-uniform skin conductivity profile. Tests conducted with body conductivity only predicted differences of a few percent in filtering when varied systematically. Fig. 4C shows the filtering effect for two versions of the taper model. The shape of the fish model's filtering curve (green trace) resembles the ones found with the taper models, either rostral to (taper of 0.05, blue trace) or caudal to (taper of 0.0178, black trace) the point of taper change (red broken line) in the fish model (see Fig. 1B for fish model geometry). This can also be understood as differences in effective distance, as a bigger taper value implies that the EO is effectively farther from the exterior skin. The slight caudal discrepancy (green *versus* black traces) is likely due to edge effects: the fish model has body tissue located between the end of the EO and the end of the tail that is not present in the taper model.

While a smooth external field may be of functional importance for the fish, as noted previously, it remains that the relevant stimuli for the skin electroreceptors is transdermal potential (Migliaro et al., 2005). It is thus reasonable to assume that a uniform transdermal potential would be of greater significance to the fish. We calculated the energy of the transdermal potential and found that it was equally 'smoothest' in the head region (data not shown). Its shape was similar to the external potential energy curve shown in Fig. 4B (green trace), although its peak was shifted rostrally. This can be understood by comparing the external and internal potentials in Fig. 4A. At the tail end, both the internal and external potentials are 'rough', but the difference between them is relatively uniform.

Voltage divider

Previous studies have likened the fish to a voltage divider (Rasnow, 1996; McAnelly et al., 2003), and Fig. 4D characterizes the accuracy of such an assumption for the first time. Transdermal potentials calculated for the taper model (simulated, blue trace) and for the ideal voltage divider

(theoretical, green trace), as well as the difference between these two quantities (red trace), are shown as a function of normalized EO length for a 5-cycle sinusoidal current density (taper model; see Materials and methods for details). A taper of 0.05 was chosen, as this is the taper that makes up the longest segment, approximately 25%, of the fish model's body. Both the simulated and theoretical curves have the same quasi-sinusoidal shape, although their amplitudes differ. The match between these two curves is especially good towards the tail. On the whole, this analysis validates the assumption that the fish body functions as an ideal voltage divider.

Electric image characterization
Effect of object location on electric images

As in several previous studies (Hoshimiya et al., 1980; Rasnow, 1996; Rother et al., 2003; Chen et al., 2005; Migliaro et al., 2005), we have characterized the electric images produced by simple (circular cross-sections) conductive objects. The effects of different lateral and rostro-caudal object locations on electric image shape are displayed in Fig. 5. The electric image gets smaller (in amplitude) and wider, as the object is moved away laterally from the fish (Fig. 5A). The image amplitude increases (in absolute terms) and then decreases, as the object moves caudally (Fig. 5B). Most of the electric images shown in Fig. 5B are bimodal in nature: they have a negative rostral peak and a positive caudal one. These images become increasingly more bimodal towards the tail. Also, the distance between successive negative peaks diminishes caudally, even though the different traces are for regularly spaced object locations (as shown in the inset). This signifies that the offset between the object's location and the location of the electric image's dominant peak on the skin varies with rostro-caudal location.

Bimodal electric image characterization

The electric images shown in Fig. 5 are similar to some of those found experimentally (von der Emde et al., 1998; Chen et al., 2005) and numerically using different modeling techniques (Hoshimiya et al., 1980; Caputi et al., 1998; Migliaro et al., 2005). However, some qualitative differences exist. In order to investigate these differences, normalized electric images (Fig. 6B), which were produced by a rostro-caudally centered metal sphere, were calculated for three separate current densities (Fig. 6A): a 1-cycle sinusoidal current density, the optimal skewed current density, as well as a unimodal, pulse-like current density similar to that found in pulse-type electric fish (e.g. Migliaro et al., 2005). The main differences in image shape are a variation in the caudal trough size and discrepancies in the location of the rostral and caudal peaks.

Three points are specified in Fig. 6B in order to better characterize the electric image's bimodal shape: the location of the rostral (xR) and caudal (xC) peaks, as well as the location of the null potential (x0) found between these two peaks. It should be noted that other characteristic points could be of importance for other EOD phases or for different rostro-caudal

object locations (see Fig. 5); however, these were not considered.

The offset between the object and image locations, as observed in Fig. 5B, was characterized in Fig. 7. Tests were carried out using the box model with 1-cycle sinusoidal (Fig. 7A,B) and skewed (Fig. 7C,D) current densities (for reference, see also Fig. 6A). These figures show that the locations of the electric image's characteristic points (xR, $x0$ and xC) change as a function of rostro-caudal object location. The solid black line (identity line) indicates where the location of the image at the skin corresponds exactly to the location of the object. For the sinusoidal current density (Fig. 7A), xR (blue trace) is closest to the object's location for the first rostral third of the fish body, $x0$ (red trace) is closest to it for the middle third, and xC (green trace) is closest to it for the last, caudal third of the body (the black broken lines delimit these zones). This indicates that either the rostral or caudal peak of the bimodal electric image is located closest to the object's

position, depending on whether the object is located close to the head or near the tail. A similar phenomenon occurs for the skewed current density (Fig. 7C), although in this case the bimodal electric image's rostral peak is closest to the object's actual location over a wider range of the fish's body. It should be noted that for a specific rostro-caudal object location, the electric image's amplitude, at this point, is zero (intersection of solid black and red curves).

The absolute amplitudes of the rostral and caudal peaks of the bimodal electric image as a function of rostro-caudal object location are shown for sinusoidal (Fig. 7B) and skewed (Fig. 7D) current densities. Here it can be seen that image amplitude is roughly proportional to the EO potential; hence,
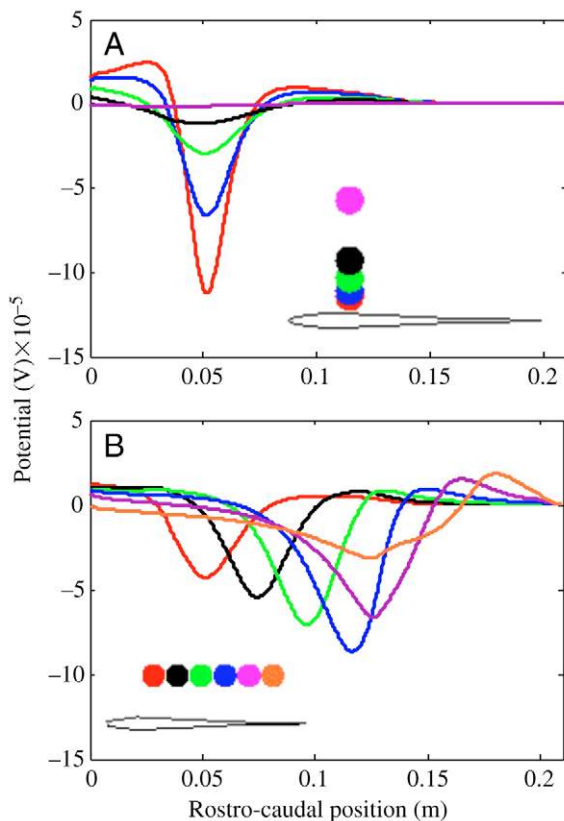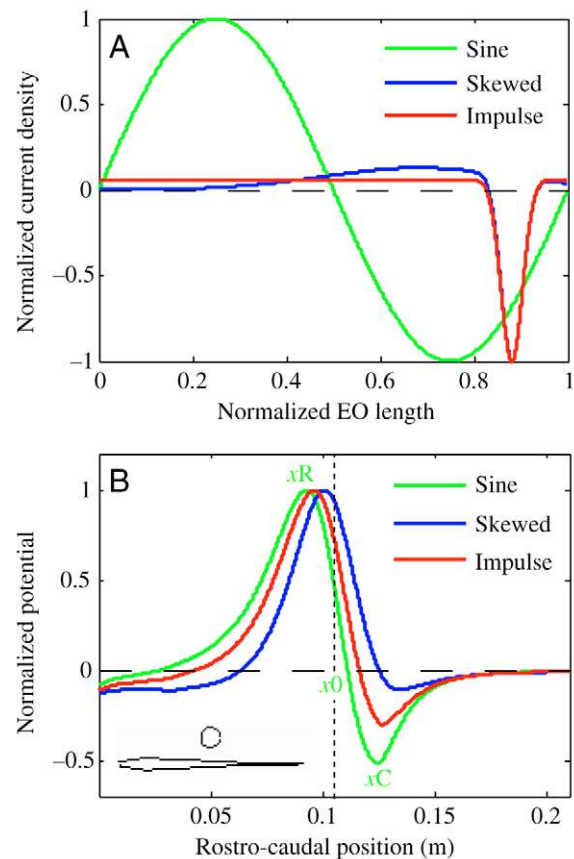

Fig. 5. Effect of object location on electric images (fish model). (A) Electric images for an object located 2 cm (red), 2.5 cm (blue), 3.5 cm (green), 5 cm (black) and 10 cm (pink) lateral of the fish's midline (5 cm caudal from the tip of the head). The electric image is calculated as the change in transdermal potential caused by the object. (B) Electric images for an object located 5 cm (red), 7.5 cm (black), 10 cm (green), 12.5 cm (blue), 15 cm (pink), 17.5 cm (orange) caudal from the start of the head at a lateral distance of 3 cm (from the fish's midline). The simulated object for A and B is a metal disc (brass; conductivity=2.13×10^7 S m^{-1}; 1 cm radius).

Fig. 6. Effect of EO current density profile on electric images (fish model). (A) Normalized current densities *versus* normalized EO position. The green trace shows the 1-cycle sinusoidal current density; the blue trace shows the optimal skewed current density (sum of two Gaussian curves); the red trace shows the 'impulse' current density (single Gaussian function offset in order to have a mean of zero). All current densities are zero-mean. (B) Normalized electric images produced by a metal disc located in the middle of the fish (black vertical line), 3 cm lateral from the midline (see inset), for skewed (blue), impulse (red) and sinusoidal (green) current density profiles. The green markers 'xR', '$x0$' and 'xC' illustrate the 'x' or rostro-caudal positions of the three points that characterize bimodal electric images: the rostral peak, the zero-crossing (located between rostral and caudal peaks) and the caudal peak, respectively.
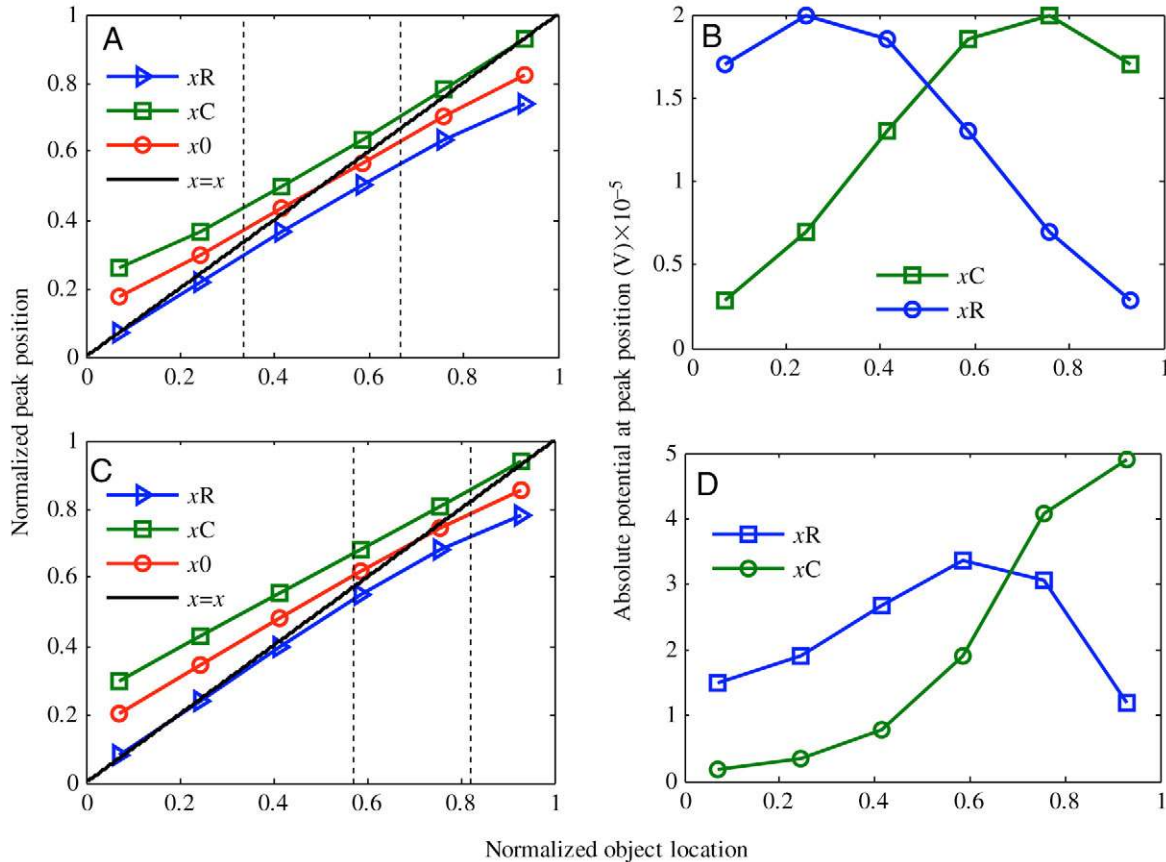
Fig. 7. Positions and amplitudes of the bimodal electric image's characteristic points ('*x*R', '*x*0' and '*x*C') for different rostro-caudal object locations (box model; optimal uniform skin conductivity; object centered 3 cm away from the fish's midline). (A,C) Normalized peak positions for sinusoidal (A) and skewed (C) current densities. Peak positions and object locations are normalized with respect to EO coordinates, with the rostral side corresponding to zero. Blue and green traces are the positions of the rostral and caudal peaks, respectively, while red traces show the positions of the zero-crossings. The solid black curve shows the identity line, where the location of the electric image's dominant peak at the skin corresponds exactly to the rostro-caudal location of the object. Black broken lines delimit zones in which certain characteristic curves are closest to the solid black trace: e.g. in C, the blue trace (*x*R) is closest to the identity line in the rostral zone, i.e. the bimodal image's rostral peak is closest to the object's actual location in this zone. (B,D) Absolute potentials of the bimodal electric image's rostral and caudal peaks for sinusoidal (B) and skewed (D) current densities. Blue traces show absolute potential values for the rostral peak while caudal peak values are shown in green.

the locations of the two amplitude peaks are approximately the same as the locations of the two peaks in a given current density profile (for both profiles). It should be noted that the potentials would have been relatively smaller in the tail region, had the non-uniform skin conductivity profile been used instead of the uniform one.

The effect of skin conductivity profile on electric image shape is studied with the box model in Fig. 8. The image due to the 'real', non-uniform skin conductivity profile (green trace; Fig. 8A) either resembles the one obtained with the uniform head conductivity (0.00025 S m^{-1}; red trace) or the one obtained with the uniform tail conductivity (0.0025 S m^{-1}; blue trace), depending on rostro-caudal location. The electric image in the middle region shows a transition from the image obtained with one of the uniform conductivities to the other. From this figure, it is also apparent that, as expected, the electric image's amplitude decreases as skin conductivity increases.

In Fig. 9 we show the bimodal electric images produced by different-sized objects as a function of lateral distance (of the object centers), using the box model (with skewed current density and uniform skin conductivity). Fig. 9A,C show un-normalized (actual amplitudes) and normalized (with respect to the caudal peak's amplitude) bimodal electric images, respectively, produced by three disc-like objects of different diameters. The amplitude (or peak-to-peak potential) of the electric image produced by the 2 cm object (Fig. 9A, red trace) is the largest since all the objects were centered at the same lateral distance of 4 cm; therefore, this object's edge was closest to the skin layer and thus affected the image more. The normalized bimodal electric images, however, are all very similar (Fig. 9C). Fig. 9B shows how the peak-to-peak amplitudes of the electric images change as a function of lateral object distance for the three objects: the curves are separated one from another by approximately an order of magnitude (e.g.
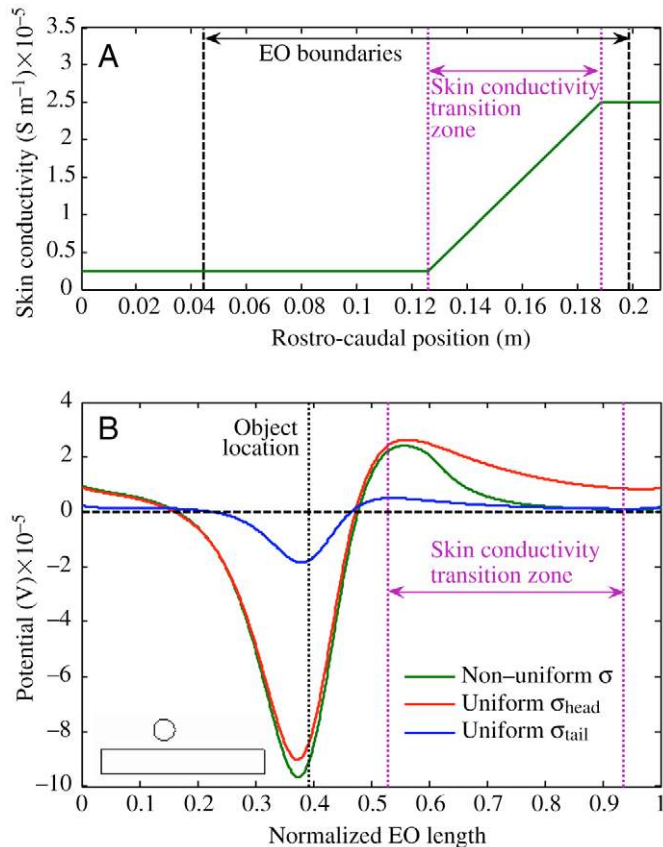
Fig. 8. Effect of skin conductivity on electric image shape (box model; skewed current density). (A) Optimal non-uniform skin conductivity profile, which has a low 0.00025 S m^{-1} conductivity at the head, a high 0.0025 S m^{-1} conductivity in the tail region and a linear conductivity increase between the two constant conductivity regions (delimited by pink dotted lines). Black broken lines delimit the EO. (B) The electric images produced by a 1 cm-radius metal object located at 0.39 along the normalized length of the EO, 3 cm lateral to the fish's midline (black dotted line; see inset) for different values and shapes of skin conductivity are shown. Green trace shows the electric image obtained with the non-uniform skin conductivity. Red and blue traces show the electric images obtained with uniform skin conductivities of 0.00025 S m^{-1} (σ_{head}) and 0.0025 S m^{-1} (σ_{tail}), respectively.

note peak-to-peak differences at black dotted line). This is in agreement with previous studies that have reported a similar correspondence between un-normalized image amplitude and lateral object distance (Heiligenberg, 1975; Bastian, 1981; Rasnow, 1996). Thus, the fish cannot unambiguously determine lateral object distance using this measure. This is because small objects placed near the fish's body may create electric images that have the same amplitude as large objects placed farther away from the fish. On the other hand, our analysis shows that the difference between the rostral and caudal peak locations (defined here as 'delta') varies consistently with lateral object distance for all three objects (Fig. 9D) and could therefore be used by the fish to unambiguously measure lateral object distance. The black

broken line in Fig. 9B,D shows the lateral distance (4 cm) for which the electric images in Fig. 9A,C were calculated. It should be noted that the results shown for the box model also hold for the fish model (not shown). However, the caudal peaks in the fish model are smaller because of the increased conductivity in the tail section (due to the nature of the non-uniform skin conductivity profile).

Fig. 10 shows the same set of panels as in Fig. 9, except that lateral distance is now calculated as a function of the object's edge, instead of the object's center. The 0.5 cm radius (blue) and 1.1 cm radius (green) objects were moved closer to the skin layer in Fig. 10A,C so that their edges were at 2 cm from the midline (same distance as the 2 cm-radius object). The amplitudes have therefore increased for these two objects since they are closer to the skin surface (Fig. 10C). There are, however, bigger differences between the normalized electric images of the differently sized objects, compared to when lateral distance is measured from the object's center. This is reflected in Fig. 10D, where one can see that the delta values no longer vary consistently with lateral distance for the three distinct objects. Indeed, this measure seems no more accurate in determining lateral distance of an object's edge than the peak-to-peak potentials shown in Fig. 10B. These results suggest specific predictions for the localization of objects of different sizes (see Discussion).

Discussion

In this paper, we have constructed three finite element models in order to study the electric field generated by the weakly electric fish, *A. leptorhynchus*. We have shown, quantitatively, that the relatively homogenous field in the rostral half of the body is due to the filtering effects of the tapered body shape, and have validated the previous assumption that the fish body acts as an ideal voltage divider. We have also characterized the bimodal electric images produced by simple objects in order to gain further insight into how these fish electrolocate objects. While these images are very similar to those calculated using different models (Hoshimiya et al., 1980; Caputi et al., 1998; Migliaro et al., 2005), there are some potentially important differences.

Electric field modeling

Our two-dimensional, realistic electric field model (referred to as the 'fish' model; see Fig. 1B) reproduces many spatial aspects of the fish's self-generated EOD potential (Fig. 3). For instance, the model duplicated the electric field's dipolar nature and rostrally leaning zero-potential line. The model was also very accurate near the fish. In particular, the rostral part of the field, where most electroreceptors are located and hence where active electrolocation is thought to be mediated (Knudsen, 1975; Carr et al., 1982), has a very low error based on comparisons with experimental data (~10%, which is comparable to that found in a recent study) (Chen et al., 2005). The high potentials and field decay in the tail region, however, were not reproduced with such a low error. This is possibly due
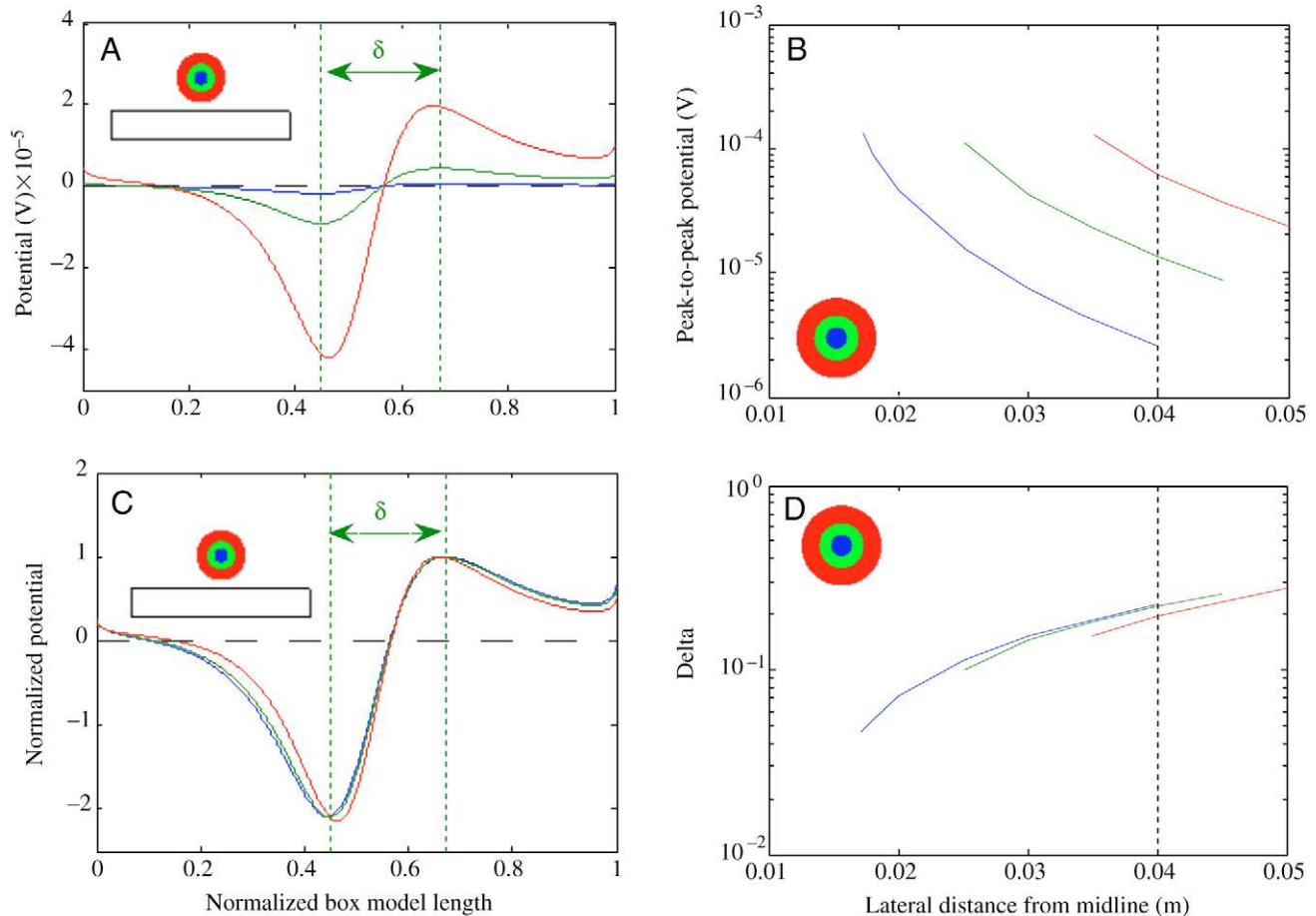
Fig. 9. Effect of object size and lateral distance on bimodal electric images (box model; skewed current density; optimal uniform skin conductivity). Lateral distance is measured with respect to object centers. (A) Un-normalized (actual amplitudes) and (C) normalized (with respect to the caudal peak's amplitude) electric images produced by three different-sized metal objects located half way along the fish's body, 4 cm away from the midline: 0.5 cm (blue), 1.1 cm (green) and 2 cm (red) radius (see inset). Both images are plotted *versus* the normalized box model length, in which the rostral side corresponds to zero. (B) Peak-to-peak potentials of the electric images found in A as a function of lateral distance away from the fish's midline for the three different objects (object sizes same as in A; see inset). (D) Delta, defined as the difference between the rostral and caudal peak locations, found in either A or C, as a function of lateral distance from the fish's midline for the three different objects; delta for the 1.1 cm object is shown in A and C. Black broken lines in B and D show the distance (4 cm away from the fish's midline) at which the objects were located for the images shown in A and C.

to the two-dimensional nature of the model in which the third spatial dimension does not contribute to the mid-planar field (see also Assad, 1997). Also, the error between our model and the experimental data does increase further away lateral to the fish. This is because potential values become very small in the far field and hence percent differences can become very large, even though the absolute errors are not large (see e.g. Fig. 3C). Fig. 3D,E show, however, that the field's fall-off is qualitatively similar between the model and the data. Therefore, we consider that results that were shown for lateral distances at which the error is larger are still valid, at least qualitatively.

The effects of EO, body and skin conductivity on external potential were studied directly and independently using the two geometrically simple models ('taper' and 'box' models; see Fig. 1C,D). The taper model also allows for an independent

study of the fish's geometry. Each model was simple to implement, using the finite element software COMSOL Multiphysics. The models are also computationally fast, solving a mesh containing 89 817 nodes in 7.6 s (on an IBM computer with a 3.2 GHz Intel Xeon processor). With its realistic electric fish geometry and parameters, the fish model presented in this paper is also an improvement over previous finite element models (Heiligenberg, 1975; Hoshimiya et al., 1980). In particular, compared with the FEM model done (Hoshimiya et al., 1980), our model is more realistic morphologically (rather than ellipse-like) and has a skin thickness approximately 30× smaller (and in the range of the measured thickness). Our EO current density was also distributed rostro-caudally along an EO, rather than a two-point dipole used in the previous model. These improvements were enabled in part by our access to increased computational power.
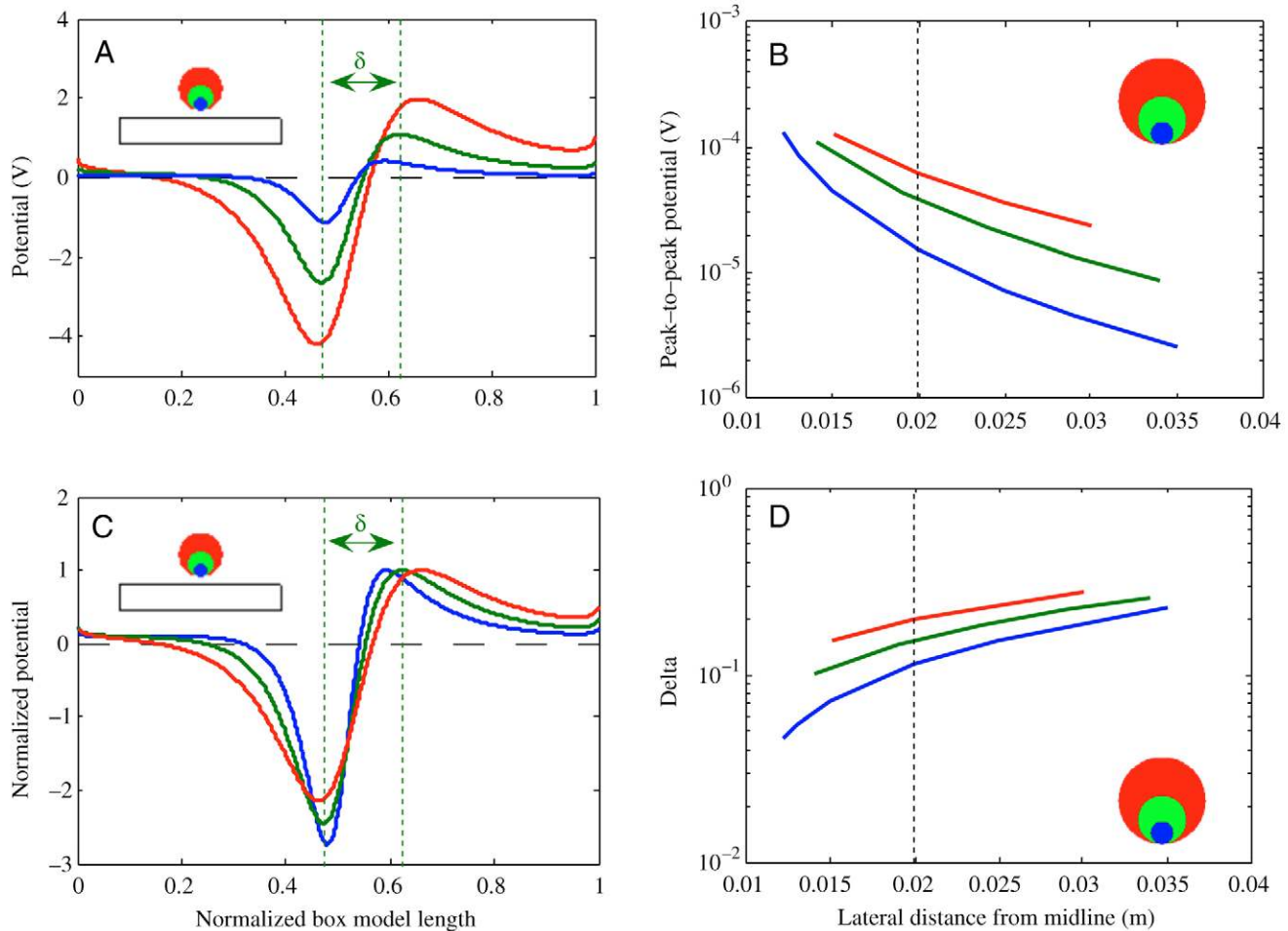
Fig. 10. Effect of object size and lateral distance on bimodal electric images. All panels are the same as in Fig. 9 except that lateral distance is measured here with respect to the object's edge. (A) Un-normalized and (C) normalized electric images produced by three different-sized metal objects located half way along the fish's body, with the object edges 2 cm away from the midline: 0.5 cm (blue), 1.1 cm (green) and 2 cm (red) radius (see inset). Red traces are the same as in Fig. 9A,C since a lateral edge distance of 2 cm for the 2 cm-radius object corresponds to a lateral object center distance of 4 cm. (B) Peak-to-peak potentials of the electric images found in A as a function of lateral distance away from the fish's midline for the three different objects (object sizes same as in A; see inset). (D) Delta found in either A or C, as a function of lateral distance from the fish's midline for the three different objects; delta for the 1.1 cm object is shown in A and C. Black broken lines in B and D show the distance (2 cm away from the fish's midline) at which the objects were located for the images shown in A and C.

The model's main shortcomings are that it is two-dimensional and that it does not reproduce the potential in the far-field and in the tail region. Also, the model currently only simulates the EOD potential for a single phase of the EOD cycle [as in other recent models (see, for example, Chen et al., 2005)]. However, the model could easily be extended to other phases by modifying the shape of the EO current density appropriately.

The parameters that provide the best fit to Assad's experimental data are in the range of those measured or predicted in the literature. An average body conductivity of 1 S m^{-1} was reported (Scheich and Bullock, 1974), whereas our optimal value is 0.356 S m^{-1}. The optimal EO conductivity, 0.927 S m^{-1}, is also very similar. Skin conductivity measurements have shown rostro-caudal variations along the fish's body (Scheich and Bullock, 1974; Assad, 1997), and other numerical modeling studies have used a three-component

skin conductivity profile in order to model this inhomogeneity (Heiligenberg, 1975; Hoshimiya et al., 1980; Assad, 1997). We have also concluded that this profile (Fig. 8A) results in more accuracy, in comparison with uniform skin conductivity profiles. However, we found that in contrast to these previous studies, such a profile was not necessary to reproduce the rostrally leaning zero-potential line (Fig. 3). Thus, for some modeling studies, a uniform conductivity could be used to simplify the models without loss of generality. Here, a uniform skin conductivity of 0.0017 S m^{-1} was used for studying the effects of other parameters independently (such as body geometry, for instance). The skewed current density profile (Fig. 2A) can be easily adapted to model the time-varying EOD: one only needs to change the mean and standard deviation of the two Gaussian functions in order to mimic different phases. It would be interesting to compare our

'simplistic' skewed current density profile with the experimentally measured one. However, these experiments have only been carried out, thus far, in pulse-type electric fish (Caputi, 1999).

Electric field characterization

It has been suggested that the uniform field near the head of weakly electric fish could improve their ability to resolve objects, because electroreceptors respond to current flowing perpendicular to the skin surface (Knudsen, 1975; Rasnow and Bower, 1996). We carried out several tests in order to better understand which attributes of the fish body are responsible for this uniform field (Fig. 4). We have shown that this spatial filtering is dictated mainly by the tapered shape of the body, and not only, for instance, because of a rostral current density of low amplitude [experiments in pulse-type fish have shown that the electromotive force varies along the fish's body length (see, for example, Caputi et al., 1989)]. The field is less smooth caudally because the skin is effectively closer to the EO, therefore reducing the amount of body and skin that can filter out the electric organ's potential. The smooth field in the head region is also aided by the fact that the head region of the fish lacks an EO (Caputi et al., 2002). In fact, we have seen that this region had the lowest exterior energy value (see Fig. 4A, green curve; energy rostral of vertical red line is minimal). The importance of skin and body tissues for filtering purposes had been suggested in the past; for example, Rasnow et al. hypothesized that this was the reason why the fish's EOD propagates less in the trunk (Rasnow et al., 1993). Our geometrically simple models have allowed us to study conductivity and body shape independently and to verify, for the first time, such hypotheses.

We also found that the relevant stimulus for skin electroreceptors, i.e. transdermal potential, was most uniform in the head region. It is possible that electric fish geometry has evolved, in part, to its current shape to increase the field uniformity near the fish's head. The fish's tapered body shape also contributes to the large potentials in the tail region, again due to the effective closeness of the EO and skin layer.

We have also shown that the weakly electric fish acts approximately as an ideal voltage divider (Fig. 4D). This is important since certain analytical (Chen et al., 2005) and semi-analytical models (Rasnow, 1996; Nelson et al., 2002), which treat electric images as perturbations of the simulated or measured field at the fish's exterior, are based on such an assumption. Our results indicate that this assumption is good, at least to a first order approximation (especially in the tail region).

Electric image characterization

By positioning an object at various lateral and rostro-caudal locations (Fig. 5), we were able to simulate electric images that resemble some of those found experimentally (von der Emde et al., 1998; Chen et al., 2005) and obtained with other numerical models (Hoshimiya et al., 1980; Migliaro et al., 2005). In particular, we found that electric images diminished in amplitude and widened with increasing lateral object distance (Fig. 5A), as previously reported (see Rasnow, 1996; Caputi et al., 1998). We also found that the electric image's peak-to-peak amplitude decreases with increasing skin conductivity (Fig. 8B), which is in agreement with Migliaro et al. (Migliaro et al., 2005). The changes in image shape that occur as the object is 'moved' rostro-caudally (Fig. 5B) can be explained by using the insights obtained with the geometrically simple models, some of which confirm previous findings. The image amplitude increases at first, due to the EO potential which increases caudally, but then decreases, even though the potential is still increasing towards its (absolute) maximal value. This happens because the conductivity of the skin is increasing, hence reducing the potential drop across the skin and, consequently, the image's amplitude. The electric image also widens because the object was moved on a straight line, and therefore the object-to-skin distance increases as the object moves towards the tail. The differences in electric image shape, such as trough sizes, produced by wave-type (skewed current density) and pulse-type (impulse current density) fish can also be explained, at least in part, by the distinct shapes of the EO current densities (Fig. 6).

Electric image analysis has previously been used to predict a set of electrolocation rules (Rasnow, 1996; Caputi et al., 1998; von der Emde et al., 1998). It was postulated that the fish could, in principle, compute an object's rostro-caudal location by simply using the location of the electric image's peak (Rasnow, 1996; Caputi et al., 1998) and an object's lateral distance, regardless of its size, by computing the ratio of maximal electric image slope and maximal electric image amplitude (von der Embe et al., 1998). These rules, however, were proposed in the context of either Gaussian-like (Rasnow, 1996) or 'Mexican-hat'-like (Caputi et al., 1998; von der Emde et al., 1998) images. While some of the images found here have a 'Mexican-hat'-like shape, with a dominant peak surrounded by troughs of opposite polarity on either side, we have also found that in some cases only one of these troughs was significant, resulting in two dominant peaks (Fig. 5B). We have characterized these bimodal electric images in order to see how electrolocation rules might differ for such image shapes.

In Fig. 7 we studied the bimodal electric images for different rostro-caudal object locations and found that there was an offset between object and electric image locations. Offsets were found in Rasnow's study (Rasnow, 1996), but he concluded that these were minimal with respect to the width of the electric image. We have shown here that different components of the bimodal electric image, not a single one, are closest to the object's location, as it moves rostro-caudally. When the object is near the head of the fish, the rostral peak of the electric image is closest to the object's location, while the caudal peak is closest when the object is near the tail.

One way that the fish could unambiguously determine which peak is closest to the object's location is by simply comparing the absolute amplitudes of the two peaks: the one with the

biggest amplitude indicating that it is closest to the object. The offset between the image peak location and object location could be of functional importance, possibly serving as a prediction of future object location (for an object moving rostro-caudally beside the fish). Nelson and MacIver postulated this was happening at the electrosensory afferent level, as the peak in afferent activity was located ahead of the transdermal potential peak (Nelson and MacIver, 1999). The offset in the bimodal electric image could provide another cue for future object location prediction, but would require the use of different peaks, depending on the object's direction of travel. Bacher has also suggested an algorithm capable of extracting object location using multimodal image shapes (Bacher, 1983); however, his method required the fish to know the object's shape beforehand (and was only valid for spheres). The cues suggested here are independent of object shape: the rostro-caudal object location is given by the location of the larger peak of the bimodal electric image (obtained by comparing the amplitudes of the two peaks), with the offset between peak and object location possibly serving as a future object location predictor. In fact, we have also performed the analysis shown in Fig. 9 using cube-like objects and have obtained similar results, i.e. that the fish could use delta as an unambiguous measure of lateral distance (not shown). One example clearly illustrates how bimodal electric images differ from unimodal ones; for certain object locations, the image has zero amplitude at the corresponding lateral skin position.

In Fig. 9 we studied the bimodal electric images produced by different-sized objects as a function of lateral distance. We have shown that the fish could, in principle, use the distance between the rostral and caudal peaks of the electric image (delta) in order to unambiguously determine lateral object distance, regardless of object size. The lateral distance measure presented here is different and computationally simpler than the one advanced earlier (von der Emde et al., 1998): only the locations of the two peaks need to be determined by the fish (normalization is not required). The electric fish could subsequently determine the object's size using the bimodal electric image's peak-to-peak amplitude (with the reasonable assumption that the object's conductivity does not change during the electrolocation task). Furthermore, we have seen that measuring lateral object distance from the center of objects (Fig. 9) seemed much more fruitful than measuring it with respect to the object edges (Fig. 10). This corroborates a previous study, which noted that measuring lateral object distance with respect to object center had simpler functional forms (Rasnow, 1996). It seems likely, however, that determining the distance of an object's edge would be more relevant for the fish. The fish could then, in principle, extract the edge's distance by using the delta-lateral distance curve associated with the object's center and then subtract its radius (obtained *via* the peak-to-peak potential value).

Conclusions

In order to fully understand electrosensory processing, one needs to understand the mechanisms that weakly electric fish use in order to generate electric signals, and how information is extracted from the electric images produced by surrounding objects. Many previous studies have focused on the posteffector mechanisms (Caputi and Budelli, 1995; Rother et al., 2003; Migliaro et al., 2005) and electrolocation principles (Rasnow, 1996; Caputi et al., 1998; von der Emde, 1999; Lewis and Maler, 2002; Chen et al., 2005) employed by weakly electric fish. We have gained further insight into the electric sense using a realistic model of the electric fish *A. leptorhynchus*, as well as two geometrically simple models that have allowed us to study the fish's conductivity and geometry in an independent way. We have also characterized bimodal electric images and seen that electrolocation rules obtained with such images differ from the ones found with Gaussian-like and 'Mexican-hat'-like images. Electrolocation rules found using bimodal electric images suggest that weakly electric fish could determine an object's rostro-caudal position by using the location of the peak whose amplitude is greatest and determine its lateral distance by using the distance between the rostral and caudal peaks. More detailed behavioral studies are required to determine which rules are actually used for electrolocation. Finally, our modeling approach also sets the stage for future studies on two poorly understood aspects of the electrolocation behavior: the influence of the time-varying EOD and the nature of complex electrosensory environments.

List of symbols and abbreviations

BEM	boundary element method
BL	body length
EO	electric organ
EOD	electric organ discharge
FEM	finite element method
j	current source density
RMS	root mean square
t	thickness
Φ, *V*	potential
σ	conductivity

References

Assad, C. (1997). Electric field maps and boundary element simulations of electrolocation in weakly electric fish. PhD thesis, California Institute of Technology, Pasadena, CA, USA.

Assad, C., Rasnow, B. and Stoddard, P. K. (1999). Electric organ discharges and electric images during electrolocation. *J. Exp. Biol.* **202**, 1185-1193.

Babineau, D. (2006). Modeling the electric field and natural environment of weakly electric fish. MSc thesis, University of Ottawa, Ottawa, ON, Canada.

Bacher, M. (1983). A new method for the simulation of electric fields, generated by electric fish, and their distorsions by objects. *Biol. Cybern.* **47**, 51-58.

Bastian, J. (1981). Electrolocation. I. How the electroreceptors of *Apteronotus*

albifrons code for moving objects and other electrical stimuli. *J. Comp. Physiol.* **144**, 481-494.

Bennett, M. V. L. (1971). Electroreception. In *Fish Physiology.* Vol. V (ed. W. S. Hoar and D. J. Randall), pp. 493-574. New York: Academic Press.

Bevington, P. R. and Robinson, D. K. (2003). *Data Reduction and Error Analysis for the Physical Sciences* (3rd edn). New York: McGraw-Hill.

Caputi, A. A. (1999). The electric organ discharge of pulse *gymnotiforms*: the transformation of a simple impulse into a complex spatio-temporal electromotor pattern. *J. Exp. Biol.* **202**, 1229-1241.

Caputi, A. and Budelli, R. (1995). The electric image in weakly electric fish: I. A data-based model of waveform generation in *Gymnotus carapo*. *J. Comput. Neurosci.* **2**, 131-147.

Caputi, A., Macadar, O. and Trujillo-Cenoz, O. (1989). Waveform generation of the electric organ discharge in *Gymnotus carapo*. III. Analysis of the fish body as an electric source. *J. Comp. Physiol. A* **165**, 361-370.

Caputi, A. A., Budelli, R., Grant, K. and Bell, C. (1998). The electric image in weakly electric fish: physical images of resistive objects in *Gnathonemus petersii*. *J. Exp. Biol.* **201**, 2115-2128.

Caputi, A. A., Castello, M. E., Aguilera, P. and Trujillo-Cenoz, O. (2002). Electrolocation and electrocommunication in pulse gymnotids: signal carriers, pre-receptor mechanisms and the electrosensory mosaic. *J. Physiol. Paris* **96**, 493-505.

Carr, C. E., Maler, L. and Sas, E. (1982). Peripheral organization and central projections of the electrosensory nerves in gymnotiform fish. *J. Comp. Neurol.* **211**, 139-153.

Chen, L., House, J. L., Krahe, R. and Nelson, M. E. (2005). Modeling signal and background components of electrosensory scenes. *J. Comp. Physiol. A* **191**, 331-345.

Heiligenberg, W. (1975). Theoretical and experimental approaches to spatial aspects of electrolocation. *J. Comp. Physiol.* **103**, 247-272.

Heiligenberg, W. (1991). *Neural Nets in Electric Fish.* Cambridge, MA: MIT Press.

Hoshimiya, N., Shogen, K., Matsuo, T. and Chichibu, S. (1980). The *Apteronotus* EOD field: waveform and EOD field simulation. *J. Comp. Physiol.* **135**, 283-290.

Knudsen, E. I. (1975). Spatial aspects of the electric fields generated by weakly electric fish. *J. Comp. Physiol.* **99**, 103-118.

Lewis, J. E. and Maler, L. (2002). Blurring of the senses: common cues for distance perception in diverse sensory systems. *Neuroscience* **114**, 19-22.

Lissman, H. W. and Machin, K. E. (1958). The mechanism of object location in *Gymnarchus niloticus* and similar fish. *J. Exp. Biol.* **35**, 451-486.

MacIver, M. A., Sharabash, N. M. and Nelson, M. E. (2001). Prey-capture behavior in gymnotid electric fish: motion analysis and effects of water conductivity. *J. Exp. Biol.* **204**, 543-557.

McAnelly, L., Silva, A. and Zakon, H. H. (2003). Cyclic AMP modulates electrical signaling in a weakly electric fish. *J. Comp. Physiol. A* **189**, 273-282.

Migliaro, A., Caputi, A. A. and Budelli, R. (2005). Theoretical analysis of pre-receptor image conditioning in weakly electric fish. *PLoS Comp. Biol.* **1**, e162005.

Moller, P. (1995). *Electric Fishes: History and Behavior.* London: Chapman & Hall.

Nelson, M. E. (2005). Target detection, image analysis and modeling. In *Electroreception (Springer Handbook of Auditory Research)* (ed. T. H. Bullock, C. D. Hopkins, A. N Popper and R. R. Fay), pp. 290-317. New York: Springer.

Nelson, M. E. and MacIver, M. A. (1999). Prey capture in the weakly electric fish *Apteronotus albifrons*: sensory acquisition strategies and electrosensory consequences. *J. Exp. Biol.* **202**, 1195-1203.

Nelson, M. E., MacIver, M. A. and Coombs, S. (2002). Modeling electrosensory and mechanosensory images during the predatory behavior of weakly electric fish. *Brain Behav. Evol.* **59**, 199-210.

Rasnow, B. (1996). The effects of simple objects on the electric field of *Apteronotus*. *J. Comp. Physiol. A* **178**, 397-411.

Rasnow, B. and Bower, J. M. (1996). The electric organ discharges of the gymnotiform fishes: I. *Apteronotus leptorhynchus*. *J. Comp. Physiol. A* **178**, 383-396.

Rasnow, B., Assad, C., Nelson, M. E. and Bower, J. M. (1989). Simulation and measurement of the electric fields generated by weakly electric fish. In *Advances in Neural Information Processing Systems* (ed. D. S. Touretzky), pp. 436-443. San Mateo, CA: Kaufmann Publishers.

Rasnow, B., Assad, C. and Bower, J. M. (1993). Phase and amplitude maps of the electric organ discharge of the weakly electric fish, *Apteronotus leptorhynchus*. *J. Comp. Physiol. A* **172**, 481-491.

Rother, D., Migliaro, A., Canetti, R., Gomez, L., Caputi, A. and Budelli, R. (2003). Electric images of two low resistance objects in weakly electric fish. *Biosystems* **71**, 171-179.

Scheich, H. and Bullock, T. H. (1974). The detection of electric fields from electric organs. In *Electroreceptors and Other Specialized Receptors in Lower Vertebrates* (ed. A. Fessard), pp. 201-278. Berlin: Springer-Verlag.

von der Emde, G. (1999). Active electrolocation of objects in weakly electric fish. *J. Exp. Biol.* **202**, 1205-1215.

von der Emde, G., Schwarz, S., Gomez, L., Budelli, R. and Grant, K. (1998). Electric fish measure distance in the dark. *Nature* **395**, 890-894.

Yamashita, E. (1990). *Analysis Methods for Electromagnetic Wave Problems.* Boston: Artech House.

Zakon, H. H. (1986). The electroreceptive periphery. In *Electroreception* (ed. W. Heiligenberg and T. H. Bullock), pp. 103-156. New York: Wiley.